

# Ground electron calibration of the Gamma-ray Transient Monitor onboard DRO-A Satellite

Pei-Yi Feng,<sup>1,2,\*</sup> Zheng-Hua An,<sup>1,†</sup> Yu-Hui Li,<sup>3,‡</sup> Qi Le,<sup>3</sup> Da-Li Zhang,<sup>1</sup> Xin-Qiao Li,<sup>1</sup> Shao-Lin Xiong,<sup>1</sup> Cong-Zhan Liu,<sup>1</sup> Wei-Bin Liu,<sup>3</sup> Jian-Li Wang,<sup>3</sup> Bing-Lin Deng,<sup>3</sup> He Xu,<sup>4</sup> and Hong Lu<sup>1</sup>

<sup>1</sup>Key Laboratory of Particle Astrophysics, Institute of High Energy Physics,  
Chinese Academy of Sciences, Beijing 100049, China

<sup>2</sup>University of Chinese Academy of Sciences, Chinese Academy of Sciences, Beijing 100049, China

<sup>3</sup>Key Laboratory of Particle Acceleration Physics & Technology,  
Institute of High Energy Physics, Chinese Academy of Sciences, Beijing 100049, China

<sup>4</sup>Institute of High Energy Physics, Chinese Academy of Sciences, Beijing 100049, China

The Gamma-Ray Transient Monitor (GTM) is an all-sky monitor onboard the Distant Retrograde Orbit-A (DRO-A) satellite, with the scientific objective of detecting gamma-ray bursts in the energy range of 20 keV to 1 MeV. The GTM is equipped with five Gamma-Ray Transient Probes (GTPs), utilizing silicon photomultiplier (SiPM) arrays coupled with NaI(Tl) scintillators for signal readout. To test the performance of the GTP in detecting electrons, we independently developed a continuous-energy-tunable, low-current, quasi-single-electron accelerator, and used this facility for ground-based electron calibration of the GTP. This paper provides a detailed description of the operational principles of the unique electron accelerator and comprehensively presents the process and results of electron calibration for the GTP. The calibration results indicate that the dead time for normal signals is less than 4  $\mu$ s, while for overflow signals, it is approximately 70  $\mu$ s, consistent with the design specifications. The GTP's time-recording capability is working correctly, accurately recording overflow events. The GTP responds normally to electrons in the 0.4-1.4 MeV energy range. The ground-based electron calibration validates the design of the GTP and enhances the probe's mass model, laying the foundation for payload development, in-orbit observation strategies, and scientific data analysis.

Keywords: NaI(Tl) crystal, Electron calibration, Energy response, Deadtime testing, Gamma-ray transient probe

## I. INTRODUCTION

The first observation of the electromagnetic counterpart event GRB170817A associated with gravitational waves (GWs) marked a significant breakthrough, heralding the era of "multi-messenger, multi-wavelength" astronomy [1–4]. Since May 2023, ground-based gravitational wave detectors (LIGO, Virgo, and KAGRA) have commenced a new phase of scientific observation (O4), providing unprecedented opportunities to discover high-energy electromagnetic counterparts related to gravitational waves [5, 6].

Several dedicated instruments are used to detect gamma-ray transients, such as Konus-Wind [7], CGRO/BATSE [8], Swift [9], Fermi/GBM [10], MAXI [11], GECAM [12–14], EP [15], SVOM [16], and CATCH [17]. However, most instruments operate in low-Earth orbit (LEO), where they pass through the South Atlantic Anomaly (SAA) or high-latitude radiation zones, resulting in a complex space environment background. The Earth's magnetic field protection is relatively weak over the SAA region, allowing more radiation from outer space to penetrate and reach lower altitudes of the atmosphere, which can easily disrupt communications for satellites, aircraft, and spacecraft passing through the SAA. Additionally, LEO satellites face inevitable Earth occultation. These are significant disadvantages of LEO detection instruments. To better observe gamma-ray transients, we strongly hope to deploy detection instrument in deep space environments.

The primary scientific objective of the Gravitational wave burst high-energy Electromagnetic Counterpart All-sky Monitor (GECAM) is to detect and locate gamma-ray transients, particularly those associated with GWs and FRBs [18–21]. GECAM-A, GECAM-B, and GECAM-C (also called High Energy Burst Searcher, HEBS) have been successfully launched into LEO, achieving a series of significant scientific discoveries [22–24]. The most significant achievement is that GECAM-C detected the brightest gamma-ray burst to date, GRB20221009A, without any data saturation or other instrument-related artifacts [25–27]. To further enhance the joint monitoring and localization capabilities for gamma-ray transients, we proposed installing a Gamma-ray Transient Monitor (GTM) on the Distant Retrograde Orbit-A (DRO-A) spacecraft (Fig. 1 (a)), which was launched in March 2024 [14, 28]. GTM, also known as GECAM-D, inherits the hardware, software, and scientific operations of GECAM mission. Similar to the previous GECAM payloads [29, 30], GTM's primary scientific objectives are to monitor high-energy electromagnetic counterparts associated with GWs, GRBs, SGRs, FRBs, and other high-energy transient events. The GTM operates in a deep space orbit, offering advantages such as an unobstructed field of view free from nearby celestial body interference and a more stable space environment, making it highly valuable for monitoring high-energy transient events.

GTM is equipped with five Gamma-ray Transient Probes (GTPs), designed to detect gamma-ray transients in the energy range of 20 keV to 1 MeV. The installation positions of these five GTPs are shown in Fig. 1 (a). Comprehensive ground calibration is essential to ensure that GTPs accurately measure the spectral information of gamma-ray transient sources. These tests aim to characterize the detector's energy response, which is necessary for the reconstruction

\* Corresponding author, Pei-Yi Feng, [fengpeiyi@ihep.ac.cn](mailto:fengpeiyi@ihep.ac.cn).

† Corresponding author, Zheng-Hua An, [anzh@ihep.ac.cn](mailto:anzh@ihep.ac.cn).

‡ Corresponding author, Yu-Hui Li, [liyuhui@ihep.ac.cn](mailto:liyuhui@ihep.ac.cn).

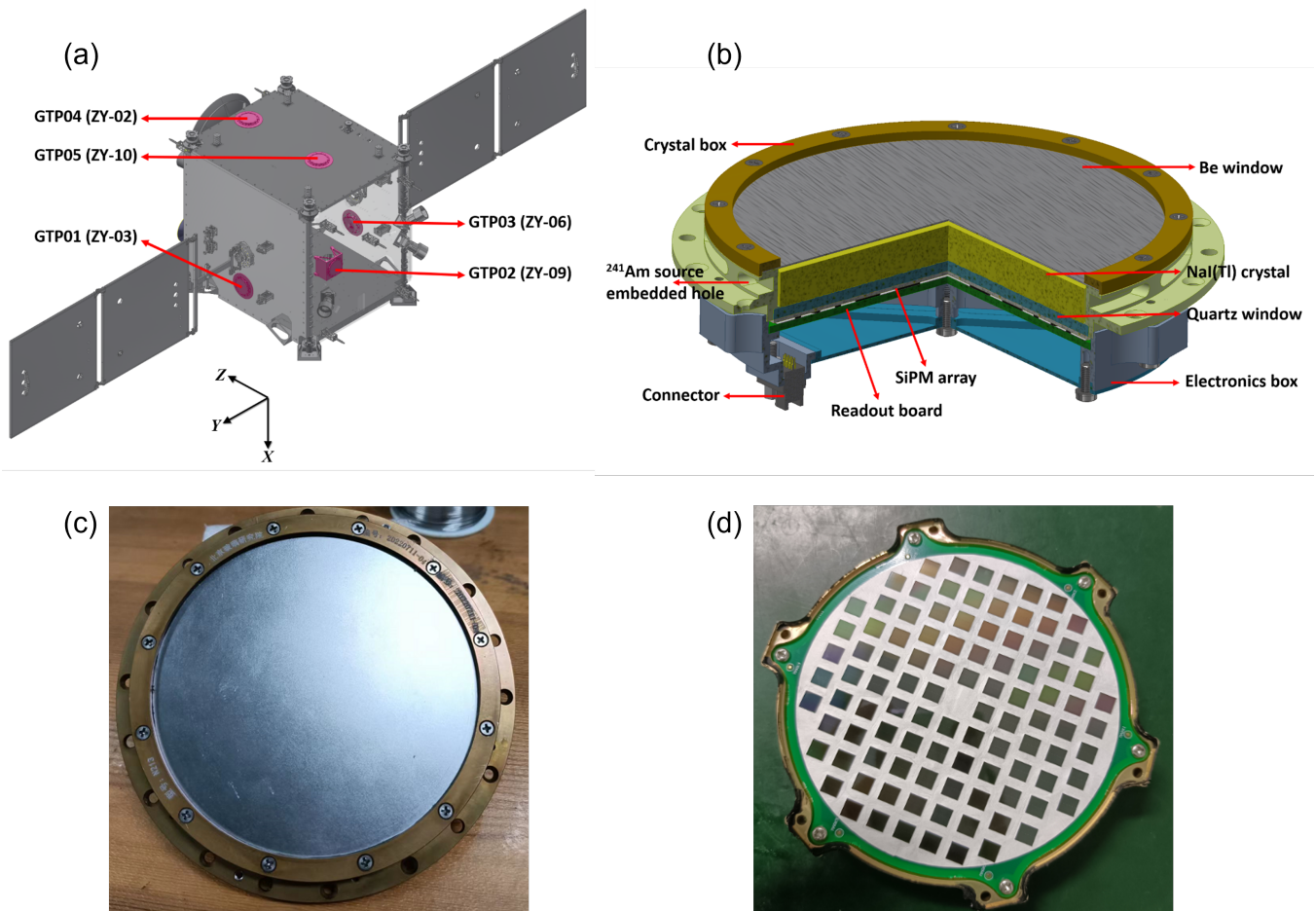


Fig. 1. (a) Overview of DRO-A satellite. GTM consists of five Gamma-ray Transient Probes (GTPs) positioned on the four sides of the spacecraft. Four standard GTPs are individually mounted on the  $\pm Y$  side (one GTP for each side) and the  $-X$  side (two GTPs), while one dedicated GTP for the  $-Z$  side. The standard GTP comprises detector components and brackets (with the brackets also doubling as radiation cooling plates), while the dedicated GTP is for science usage, whereas that with ZY is for the crystal label of detector [14]. (b) Structural diagram of GTP module onboard GTM [14]. (c) NaI(Tl) crystal encapsulation. (d) A 100-chip SiPM array and a preamplifier circuit board.

of in-flight particle flux. The ground calibration project for X-rays and gamma rays includes aspects such as time coincidence, energy response, detection efficiency, spatial response, bias-voltage response, and temperature dependence, all of which have been completed [14]. Electron calibration is also an important component of ground calibration. Although GTM's flight orbit does not pass through the SAA, it encounters a different space radiation environment in deep space, especially when passing through the Earth's magnetotail, where electron activity significantly increases. The orbital period of the DRO-A satellite is approximately thirty days, and GTM crosses the magnetotail for about three days around each full moon. The magnetotail contains a large number of charged particles, which may contribute to the GTP's background. Typical electron energy is about 1 keV, with a density of approximately  $0.1\text{-}1\text{ cm}^{-3}$ , seemingly below the detection threshold. However, magnetic reconnection frequently occurs in the magnetotail, accelerating charged particles to higher energies and contributing to GTM's background

[28]. To evaluate the GTP's performance in such a complex environment, ground calibration using high-energy electron beams is essential, focusing primarily on the dead time of overflow signals and the energy response in the 0.4-20 MeV range.

There are several operational electron calibration facilities internationally. The DAΦNE Beam Test Facility (BTF) provides an  $e^-/e^+$  beam with an energy range of 30-750 MeV, a pulse intensity from a single particle to  $10^{10}$  particles, and a maximum pulse repetition rate of 50 Hz [31]. The Medical and Industrial Radiation Facility (MIRF) at the U.S. National Institute of Standards and Technology (NIST) features a linear electron accelerator that delivers electron beams in the energy range of 7-32 MeV, with intensities from a few nA to several tens of  $\mu\text{A}$  [32]. The Joint Institute for Nuclear Research (JINR) in Russia operates the LINAC-200 linear accelerator, whose first section can provide electrons in the energy range of 10-25 MeV [33]. These electron accelerators have been used to calibrate numerous space particle detectors

[34, 35].

We are excited to report that, in this work, we have independently developed a continuous-energy-tunable, low-current, quasi-single-electron accelerator calibration facility. Located at the Institute of High Energy Physics, Chinese Academy of Sciences, this facility features unique characteristics of low current and a wide energy range, making it the only electron accelerator in China with such low intensity. This paper first provides a detailed description of the design of the GTP and the electron accelerator facility, followed by a presentation of the complete process and results of electron calibration for the GTP, and concludes with a summary. Ground electron calibration not only validated the detector's mass model and Monte Carlo simulated energy response matrix but also laid the foundation for establishing a calibration database. The detailed ground calibration ensures that the GTM can accurately and reliably monitor high-energy transient events, providing robust technical support for exploring extreme astrophysical phenomena.

## II. INSTRUMENT DESIGN AND ELECTRON BEAM CALIBRATION

This section introduces the design of the Gamma-ray Transient Probe (GTP) and the working principles of the high-energy electron accelerator calibration facility.

### A. Design of Gamma-ray Transient Probe

A single GTP (Fig. 1 (b)) installed on the GTM payload consists mainly of a NaI(Tl) crystal coupled with a 100-chip SiPM array. The NaI(Tl) crystal, with a diameter of 115 mm and a thickness of 10 mm, serves as the sensitive detection material for the GTP. For GRBs of the same brightness in identical space environments, the effective area of the GTP directly determines its sensitivity. When the number of GTPs is limited by factors such as weight, power consumption, and electronics complexity, a sufficiently large area for a single GTP can ensure the detection sensitivity for GRBs. Since NaI(Tl) crystal is hygroscopic, it must be well encapsulated. Figure 1 (b) shows a schematic of the encapsulated GTP structure. Figures 1 (c) and (d) present the packaged NaI(Tl) crystal and the SiPM readout array with the preamplifier circuit board, respectively. The SiPM is a highly sensitive photodetector that offers several advantages, including compactness, light weight, low power consumption, and the elimination of high voltage requirements. It has been successfully implemented in the gamma-ray detectors (GRD) on GECAM-A/B and GECAM-C [18, 19, 22, 36].

One of the features of the GTP is the inheritance and development of GRD technology [14, 37], using a 4.5-inch circular SiPM array instead of traditional photomultiplier tube (PMT). The SiPM array, consisting of 100 SiPM chips uniformly arranged in a circular pattern, has reflective membranes filling the gaps to improve light collection uniformity. The SiPM array is divided into two groups, each with parallel output

and an independent readout system. Offline data processing can time-coincide data from these two channels to eliminate SiPM dark noise, which is a highlight of the GTP design. Previous research concluded that a coincidence time window of 0.5-1  $\mu\text{s}$  is appropriate [14]. Therefore, for the data processing involved in this paper, a coincidence time window of 0.5  $\mu\text{s}$  is adopted.

Gamma rays enter through a 400  $\mu\text{m}$ -thick Be window and a 600  $\mu\text{m}$ -thick Teflon reflective material, interact with the NaI(Tl) crystal, and the resulting scintillation light passes through a 3 mm-thick quartz glass window to be received by the SiPMs. The SiPMs convert the light signal into an electrical signal, which is amplified by a preamplifier and connected via electrical connectors to the data acquisition system for recording. The GTP provides both energy and time information of the gamma rays for physical analysis. Additionally, a hole on the side of the GTP is designed to embed a  $^{241}\text{Am}$  radioactive source with an activity range of 500 to 800 Bq, whose decay generates a 59.5 keV gamma-ray full-energy peak used for in-orbit calibration of the GTM instrument. The design of the GTP is discussed in greater detail in previously published article [14].

### B. High-energy Electron Accelerator Calibration Facility

To meet the calibration requirements of high-energy particle detectors, especially space particle detectors, we have independently developed a continuous-energy-tunable, low-current, quasi-single-electron accelerator calibration facility, located at the Institute of High Energy Physics, Chinese Academy of Sciences. The accelerator's electron beam is generated by accelerating low-energy electrons emitted from a low-current electron gun. It can provide pulsed beams with intensities ranging from a single electron to several tens of electrons, with energies ranging from 100 keV to 50 MeV. The pulse duration can be adjusted between 1 ns and 10 ns at a maximum repetition rate of 50 Hz. This system has been used for testing and calibration of various detectors, including silicon detectors, scintillation counters, and crystal detectors.

Figure 2 shows the experimental layout of the High Energy Physics Institute's quasi-single-electron accelerator. To achieve beam energies adjustable from 100 keV to 50 MeV, the high-energy electron accelerator calibration facility's acceleration tubes are divided into two sections: a 1-meter-long tube (A1) and a 3-meter-long tube (A2). Following the 1-meter-long acceleration tube is a deflection magnet (B1) that directs low-energy beams to the side terminal of the accelerator. The low-energy range can cover beams with energies below 7 MeV. High-energy beams exceeding 7 MeV need to pass through the 3-meter-long acceleration tube after the 1-meter tube for further acceleration, then consecutively through deflection magnets B2 to B4, finally reaching the side terminal of the accelerator. The accelerator terminal is connected to a vacuum chamber, within which the GTP is positioned. Signals are transmitted through cables to an external data acquisition system (Fig 2). Figures 3 (a), (b), and (c) respectively show the physical images of the electron

accelerator tunnel, the large vacuum chamber, and the GTP calibration site.

To obtain quasi-single-electron beams, beam collimators are placed along the accelerator and at the terminal. The attenuation factor of the collimator slits, measured under normal electron beam conditions, is approximately 1/350. After the quadrupole magnet Q4 in the high-energy section, one set of horizontal and vertical beam slits is installed. After the final quadrupole magnet Q5, two sets of horizontal and vertical beam slits are installed to scrape the beam according to its angle and transverse position. The control of beam energy and energy spread at the accelerator terminal is achieved using the final 90-degree deflection magnet and the beam collimators at the end of the accelerator. Ideally, the relationship between the beam's bending radius in the magnetic field, the magnetic field strength, and the beam energy is given by Equation 1.

$$\frac{1}{\rho} [m^{-1}] = \frac{eB_0}{p} = 0.2998 \frac{B_0 [T]}{p [GeV/c]} \quad (1)$$

Here,  $\rho$  represents the electron's bending radius,  $B_0$  is the magnetic field strength, and  $p$  is the electron's momentum. To achieve accurate control of beam energy, the magnetic field distribution and excitation curve of the deflection magnet were precisely measured. This data was then used to calculate the magnet's excitation current for different beam energies, followed by particle tracking calculations for further refinement. These steps also determine the relationship between the collimator slit and the beam energy spread.

The beam distribution at the accelerator's terminal is monitored using a particle distribution detector (PDD), as shown in Fig 4(a). This detector employs thick gas electron multiplier (THGEM) technology to measure the two-dimensional spatial position of quasi-single electron beams. After the electron beam passes through a thin film window and enters the drift electric field region, ionization occurs. The ionized electrons are then amplified through multiple stages and collected by the induction readout plane. The readout plane is divided into 100 signal readout strips in both the Z and Y directions (Fig 4(b)), totaling 200 channels. Each Z and Y readout strip has a width of 0.46 mm and a spacing of 0.1 mm. The detector's data acquisition system measures the charge amount in each channel, determining the beam's incident position using the centroid algorithm. This system can perform online profile monitoring of ultra-low intensity beams. The position where the quasi-single electron beam strikes the PDD detector is uncertain. Its spatial distribution range is related to the beam's energy, count rate, average number of electrons, and the slit width. Figure 4(c) shows the centroid distribution of quasi-single electrons striking the PDD at an energy of 40 MeV, with an average of approximately 1.5 electrons. It can be seen that the width of the beam centroid variation is about 20 mm, and the root mean square (RMS) of the centroid variation for every 1000 triggers is about 4 mm.

Silicon detectors and plastic scintillator detectors are used at the terminal of the electron accelerator beam to monitor beam energy and electron count. The energy measurement range of the silicon detector is 100 keV to 2 MeV, while the

plastic scintillator detector's range is 500 keV to 5 MeV. Figure 5 shows the silicon detector and plastic scintillator detector used for beam energy monitoring. Figure 6 presents the energy spectrum of a 2.5 MeV electron beam measured with the plastic scintillator detector, clearly showing the characteristic multi-electron spectral shape.

### III. ELECTRON ENERGY RESPONSE SIMULATION

Geant4, developed by the European Organization for Nuclear Research (CERN), is a Monte Carlo (MC) application package used for simulating particle transport through matter [38, 39]. In this study, we used version 11.0.3 of Geant4 to construct a GTP detector model identical to the one described in Section II A. However, due to the blocking effect of the Be window and Teflon, the incident electrons were unable to deposit their full energy in the NaI(Tl) crystal. We specifically investigated the deposited energy spectra of the NaI(Tl) crystal to incident electrons at 18 energy points within the 0.4-20 MeV range, both with and without the Be window and Teflon. In the Geant4 simulation, the GTP was placed in a vacuum environment, and 100,000 electrons were emitted from a distance of 50 mm from the center of the GTP at a 90° incident angle. We recorded the deposited energy in the NaI(Tl) crystal for each event. The partial results are shown in Fig. 7: the red curves represent the deposited energy spectra in the NaI(Tl) crystal without the Be window and Teflon, showing a distinct full-energy peak and a plateau caused by electron scattering. In contrast, the black curves represent the deposited energy spectra with the Be window and Teflon, showing only a lower-energy electron scattering plateau. It is clearly observed from the figures that the Be window and Teflon significantly absorb the electrons' energy, and only after nearly 100 keV of energy is absorbed can the electrons penetrate the Be window and Teflon to deposit energy in the NaI(Tl) crystal.

The energy transported to the NaI(Tl) crystal after passing through multiple layers of material from a monoenergetic incident electron is not singular but forms a distribution. The interaction mechanisms between electrons and the NaI(Tl) crystal are diverse, mainly including three types: (1) multiple scattering and ionization, resulting in the deposition of the full energy; (2) partial energy deposition followed by scattering out of the NaI(Tl) crystal; (3) bremsstrahlung producing gamma photons, with three possible outcomes for these photons: (a) directly escaping the NaI(Tl) crystal, (b) undergoing a photoelectric cascade process that produces multiple Auger electrons and characteristic X-rays, or (c) undergoing Compton scattering, generating one or more Compton electrons, with secondary photons then undergoing a photoelectric cascade process.

From the simulation results, the deposited energy spectrum in NaI(Tl) crystal lacks a full-energy peak but features a continuous plateau caused by electron scattering and a most probable energy peak. The deposited energy spectra of NaI(Tl) crystal for different incident electron energies are plotted on the same graph for comparative analysis, as shown in Fig. 8.

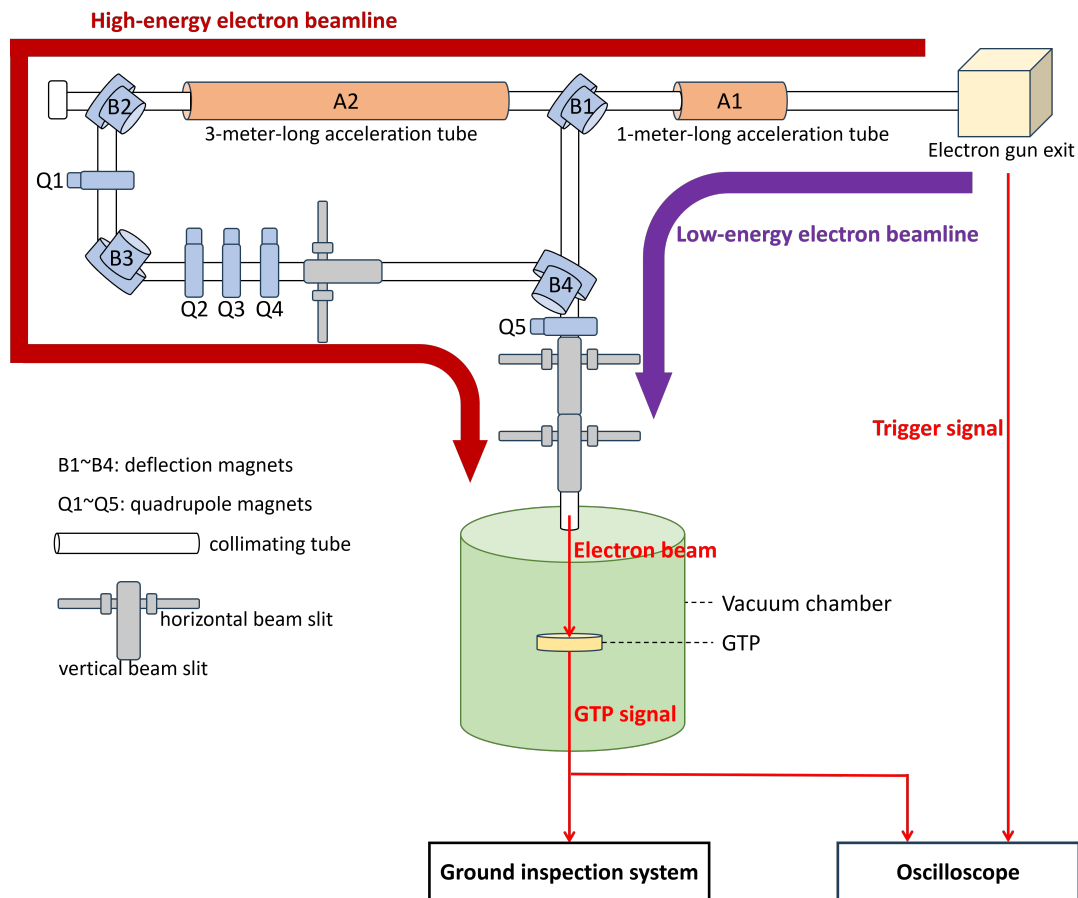


Fig. 2. Experimental layout of the quasi-single-electron accelerator, with the high-energy electron accelerator calibration facility located at the Institute of High Energy Physics, Chinese Academy of Sciences.

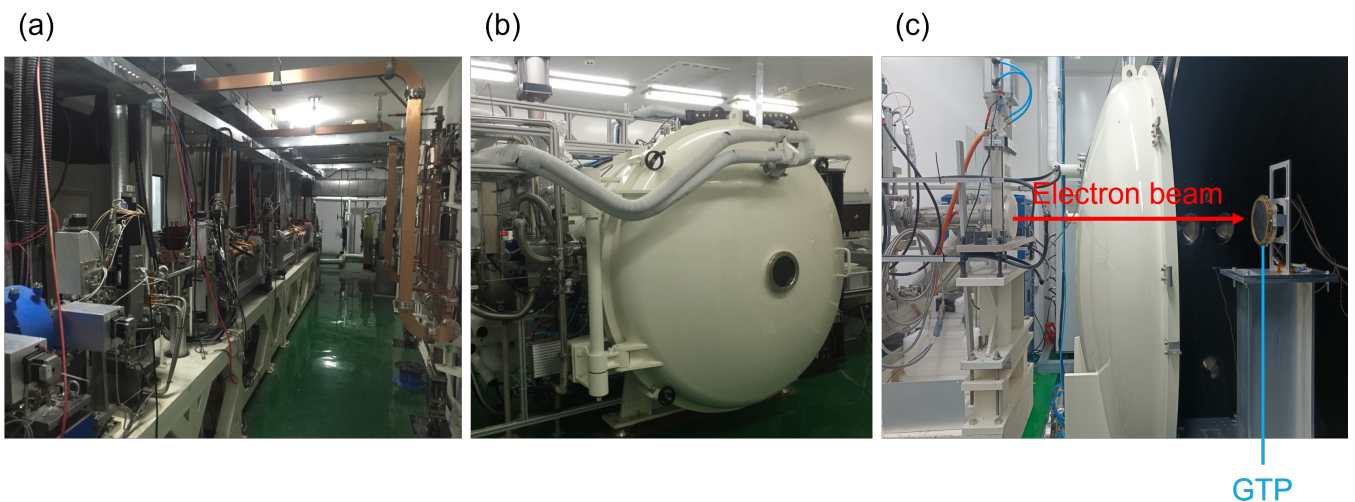


Fig. 3. (a) Electron accelerator tunnel. (b) Large vacuum chamber. (c) Electron calibration experimental site. The GTP is placed inside the vacuum chamber, and a laser level is used to align the positions of the GTP and the beam, with a positional deviation of approximately 2 mm between the center of the electron beam and the GTP.

As the incident electron energy increases, the most probable energy peak detected by NaI(Tl) becomes more pronounced.

However, at higher electron energies, the intensity and probability of bremsstrahlung increase, causing high-energy elec-

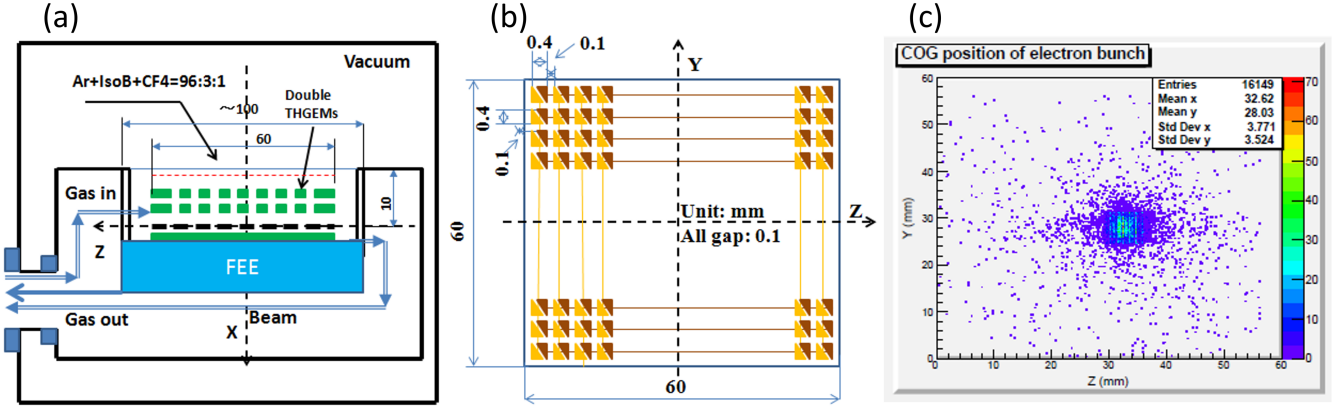


Fig. 4. (a) Composition and schematic diagram of the particle distribution detector (PDD) system. (b) Readout plane of the particle distribution detector. (c) Transverse distribution of the centroid position of the 40 MeV electron beam, based on the two-dimensional spatial monitoring results from the particle distribution detector.

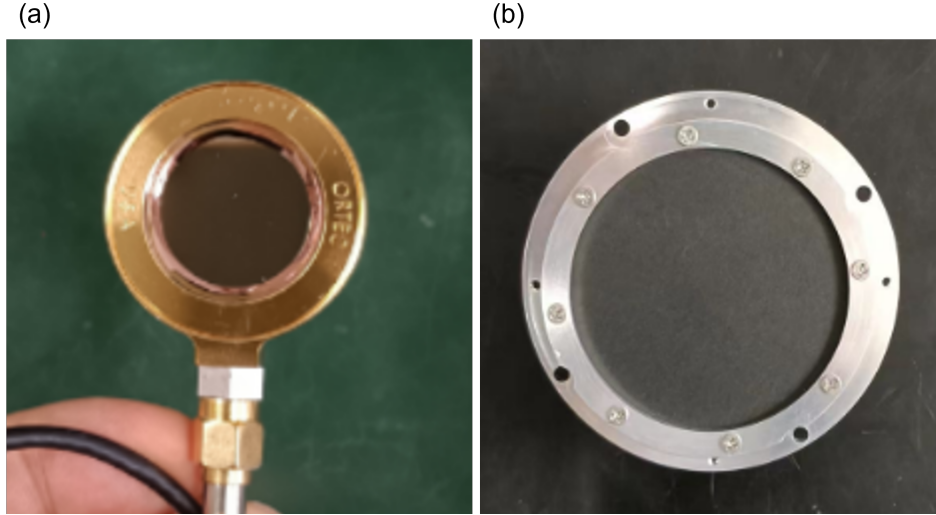


Fig. 5. Silicon detector (a) and plastic scintillator detector (b) are used to monitor beam energy and electron count.

trons to deposit only part of their energy, with the remainder escaping as gamma photons produced by bremsstrahlung. This explains why, as shown in Fig. 8 (b), the count of events in the high-energy region of the NaI(Tl) deposition spectrum is relatively low for incident electron energy of 20 MeV.

We fitted the most probable energy peaks at 11 energy points within the 0.4-1.4 MeV range using the inverse-Landau function, as shown in Equation 2. In this equation,  $MPV$  represents the most probable energy deposited by electrons in the NaI(Tl) crystal,  $\eta$  denotes the width of the inverse-Landau distribution, and  $A$  is the amplitude parameter. The fitting results for incident electron energies of 0.6 MeV and 1.2 MeV are shown in Figs. 9 (a) and (b), respectively. Figure 10 (a) illustrates the relationship between the most probable energy and the incident electron energy, which is fitted using a quadratic polynomial (Equation 3). In the subsequent Section IV B, the most probable energy obtained from the Geant4 simulation will be used to ensure the accuracy

of the energy response when presenting the energy-channel and energy-resolution relationships. The detection efficiency of the GTP is defined as the ratio of the number of events with non-zero deposited energy in the NaI(Tl) crystal to the number of incident electron events. Figure 10 (b) shows the GTP detection efficiency in the energy range of 0.2-1.4 MeV. When the incident electron energy is below 250 keV, the detection efficiency is nearly zero, but when the incident energy exceeds 500 keV, the detection efficiency surpasses 90%. For incident electron energies of 300 keV and 400 keV, approximately 24% and 75% of electron events, respectively, can penetrate the Be window and Teflon material to reach the NaI(Tl) crystal.

$$f(x; MPV, \eta, A) = A \cdot e^{-\frac{1}{2} \left( \frac{MPV-x}{\eta} + e^{\frac{x-MPV}{\eta}} \right)} \quad (2)$$

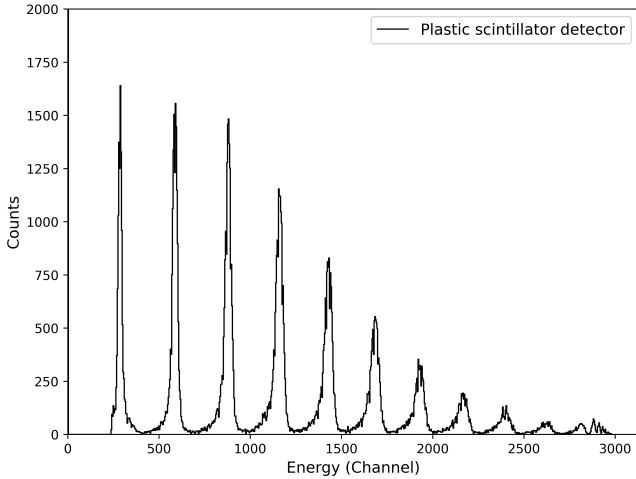


Fig. 6. Multi-electron spectrum of the 2.5 MeV electron beam measured by the plastic scintillator detector.

$$f(x) = a_0 + a_1 \cdot x + a_2 \cdot x^2 \quad (3)$$

To study the response over a continuous energy range, we simulated the energy response matrix of the GTP to both electrons and gamma photons. The G4UniformRand() function in Geant4 was used to generate random energies within the ranges of 0-2 MeV and 0-20 MeV. At a distance of 50 mm from the GTP center, 100,000 electron events and 100,000 gamma events with these random energies were emitted at a 90° incident angle. Figure 11 (a) shows the response matrix for electrons (red markers) and gamma rays (blue markers) with incident energies in the narrow range of 0-2 MeV. Significant detection counts for electrons were only observed when the incident electron energy exceeded 0.25 MeV. Due to the obstruction of the Be window and Teflon material, the maximum energy deposited by electrons differs consistently from the full-energy peak of gamma rays with the same incident energy. Figure 11 (b) shows the response matrix for the wide energy range of 0-20 MeV. When the incident energy exceeds 15 MeV, scattering and bremsstrahlung reduce the number of counts in the high-energy region of the NaI(Tl) deposition spectrum. For gamma rays with excessively high energies, the probability of directly penetrating the GTP increases significantly, resulting in a sharp decrease in full-energy deposition events.

#### IV. ELECTRON BEAM CALIBRATION RESULTS

This section presents the results of the ground-based electron calibration experiments for the GTP, focusing on two key aspects: the dead time testing in the 0.4-20 MeV range and the energy spectrum response in the 0.4-1.4 MeV range.

##### A. Deadtime Testing

In the calibration experiments, we first tested the pulse shape and energy spectrum of the GTP using the electron accelerator beam to investigate its electron response. Following the method described in Section II B, the GTP was installed in the vacuum chamber at the accelerator terminal, and the signal was connected to the data acquisition system outside the chamber via cables (Fig. 2). The chamber door was then closed, and a vacuum was created (Fig. 3 (c)). The electron accelerator provided the beam and a trigger pulse, allowing the observation of the electron beam pulse signal from the GTP on an oscilloscope. Figure 12 displays the pulse waveform of the quasi-single electron beam. Figure 12 (a) shows the normal signal detected by the GTP, with a pulse width of 2-3  $\mu$ s. To ensure the signal returns to the baseline, the dead time of the GTP for normal events is designed to be a fixed 4  $\mu$ s. In Fig. 12 (b) and (c), the pulse width exceeds 4  $\mu$ s. These cases are referred to as overflow signals, in which only the dead time duration is recorded, while the amplitude is not. The designed dead time for such signals in the GTP is 70  $\mu$ s.

For electron beams with energy exceeding 2 MeV, the dead time is analyzed mainly by testing the waveform of the GTP signals. When encountering a large deposited energy, the GTP generates an overflow signal, with the undershoot and baseline recovery time primarily influenced by the slew rate of the preamplifier chip. Figure 12 (c) shows the overflow pulse signal generated by the 20 MeV electron beam on the GTP, with a dead time of approximately 70  $\mu$ s, consistent with the designed value of the data acquisition system. The time interval spectrum of the GTP was analyzed using a 50 Hz, 0.7 MeV electron beam. It was found that the time intervals of events detected by the GTP were multiples of 20 ms, indicating that the GTP's time-recording capability is working correctly. The time interval of the accelerator electron beam is 20 ms, with a time jitter of less than 60  $\mu$ s, while the GTP data acquisition system records with a time precision of approximately 100 ns.

##### B. Energy Response

We used an electron accelerator to test the energy response of the GTP for electron beams in the 0.4-1.4 MeV energy range. The calibration experiment was conducted at 100 keV intervals, with a total of 11 tested energy points and at least 10,000 counts per point. During the experiment, at least five sets of background data were collected. Figure 13 (a) shows a background spectrum detected by the GTP, where the 59.5 keV full-energy peak of the embedded radioactive source <sup>241</sup>Am is clearly visible. From the background data, it is observed that the noise level of the GTP is slightly high, but it does not affect the electron calibration measurements, and the GTP's temperature is relatively stable.

However, due to the high gamma-ray background count rate in the environment and the low count rate of the electron beam, the energy peak of the electrons was not distinct. To address this issue, we not only increased the test duration

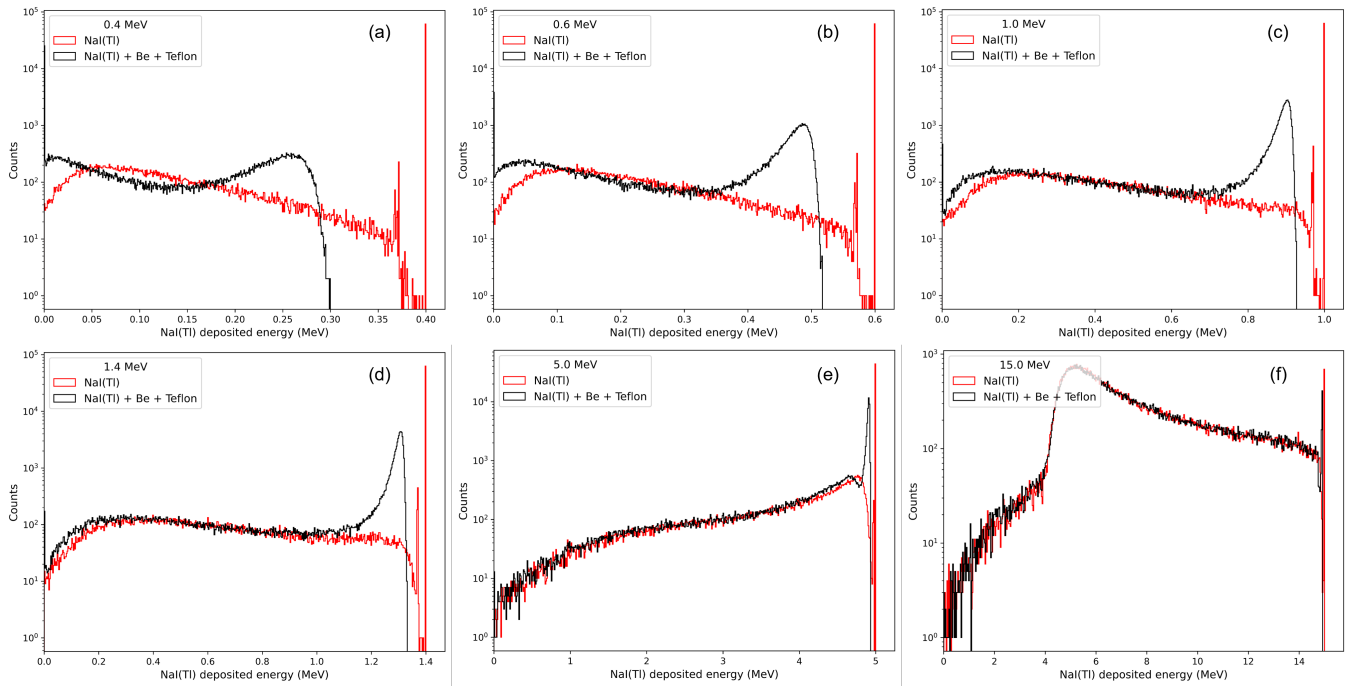


Fig. 7. Deposited energy spectra detected by the GTP in two scenarios: with and without the Be window and Teflon material. The incident electron energies are 0.4 MeV (a), 0.6 MeV (b), 1.0 MeV (c), 1.4 MeV (d), 5.0 MeV (e), and 15.0 MeV (f).

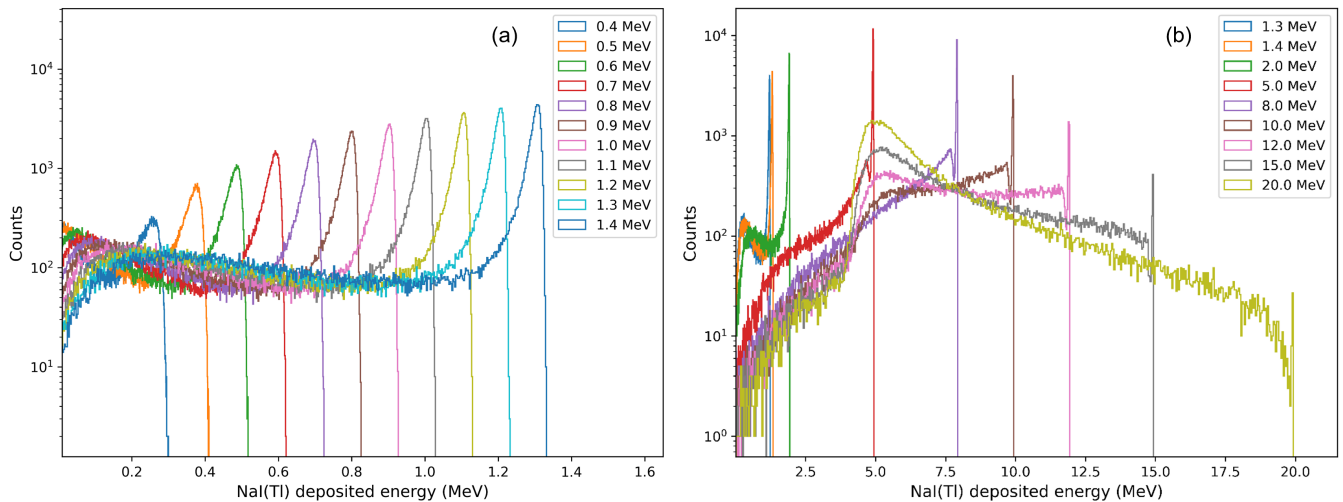


Fig. 8. Deposited energy spectra of GTP (with the Be window and Teflon) for electrons in the low incident energy range of 0.4-1.4 MeV (a) and high incident energy range of 1.3-20 MeV (b).

(3600 s per energy point) but also filtered the electron events based on time intervals of  $20 \text{ ms} \pm 0.06 \text{ ms}$ ,  $40 \text{ ms} \pm 0.06 \text{ ms}$ ,  $60 \text{ ms} \pm 0.06 \text{ ms}$ ,  $80 \text{ ms} \pm 0.06 \text{ ms}$ , and  $100 \text{ ms} \pm 0.06 \text{ ms}$ . Figures 13 (b) and (c) show the deposited energy spectra of the 0.7 MeV electron beam in the GTP before and after event selection, respectively. In the post-selection electron spectrum, the characteristic features of single-electron dominance with some double-electron components, as well as the platform component caused by electron scattering, are clearly visible. Figure 14 shows the time interval spectrum of the 0.7

MeV electron beam at 50 Hz after event selection. It is evident that the interference from gamma events and noise was effectively eliminated, isolating the electron beam events of interest for this study.

For the data collected by the GTP in the 0.4-1.4 MeV energy range, the event selection described above was applied, and the same process was performed for the background data. By subtracting the background from the deposited electron energy spectrum, a filtered energy spectrum was obtained, referred to as the net deposited energy spectrum. Figure 15



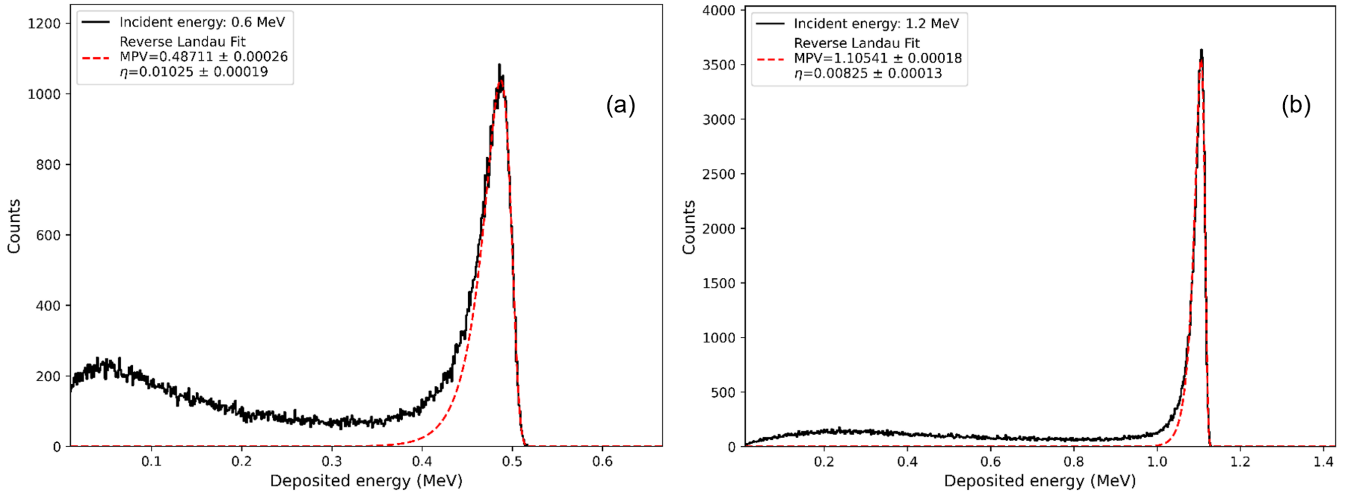


Fig. 9. Reverse-Landau fit results of the deposited energy spectra for GTP with incident electron energies of 0.6 MeV (a) and 1.2 MeV (b) are presented, where the MPV represents the most probable energy deposited in the GTP.

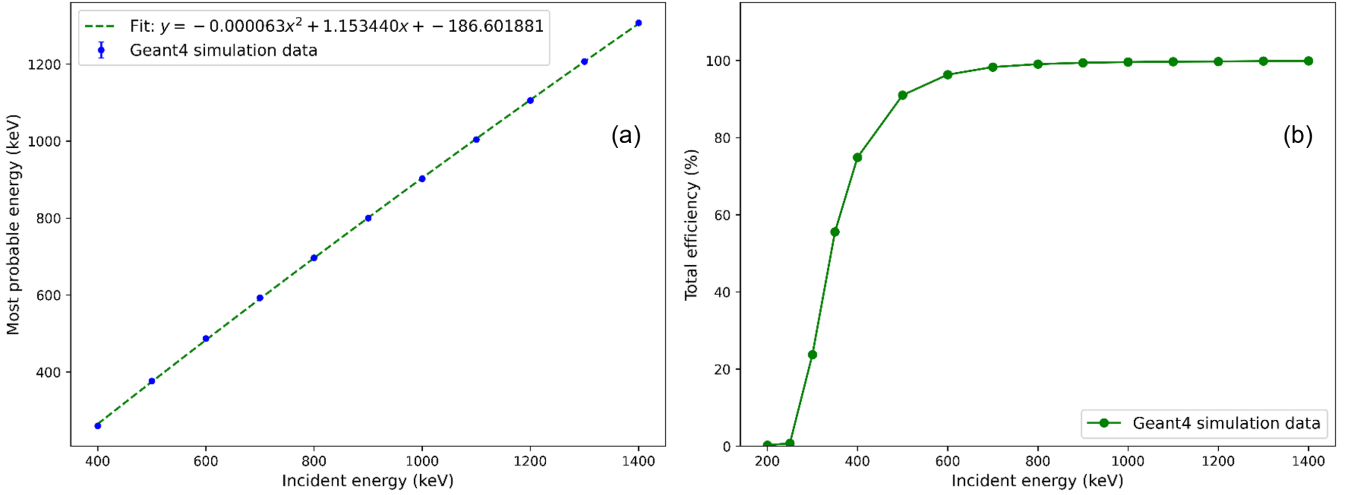


Fig. 10. (a) Relationship between the incident electron energy and the most probable energy. (b) Geant4 simulation results of the GTP's detection efficiency.

shows the net deposited energy spectra at partial energy points and the corresponding Gaussian fitting results (Equation 4). These fitting results, such as the centroids of energy peak ( $\mu$ ) and standard deviations ( $\sigma$ ), provide a basis for establishing the energy-channel (E-C) relationship and energy resolution of the GTP for electrons. Figure 16 (a) presents the E-C relationship of the GTP for electrons, along with the curve fitted using a quadratic polynomial (Equation 3). Figure 16 (b) shows the energy resolution of the GTP. Here, the energy resolution is represented by the full width at half maximum ( $\text{FWHM} = 2.355 \cdot \sigma$ ), and its uncertainty is calculated using the error propagation formula.

$$f(x) = A \cdot e^{-\frac{(x-\mu)^2}{2\sigma^2}} \quad (4)$$

It is important to note that electrons deposit energy while

passing through the Be window and Teflon reflective materials, resulting in a deposited energy in the NaI(Tl) crystal that is lower than the beam energy. Therefore, the horizontal axis in Fig. 16 needs to be corrected to the most probable energy of electrons, as determined by the Geant4 simulation described in Section III. In Fig. 16 (a), the lowest incident energy is 400 keV, corresponding to a most probable deposited energy of 259.8 keV in the GTP, while the highest incident energy is 1400 keV, corresponding to a most probable deposited energy of 1307.4 keV. The figure shows that the GTP's response to electrons increases nearly linearly, indicating that the detector's response is normal and meets the design expectations. Due to detection threshold constraints, the electron spectrum measured at an incident energy of 400 keV is incomplete. Therefore, Fig. 16 (b) only presents the energy resolution for incident energies in the range of 500-1400 keV. Based on the

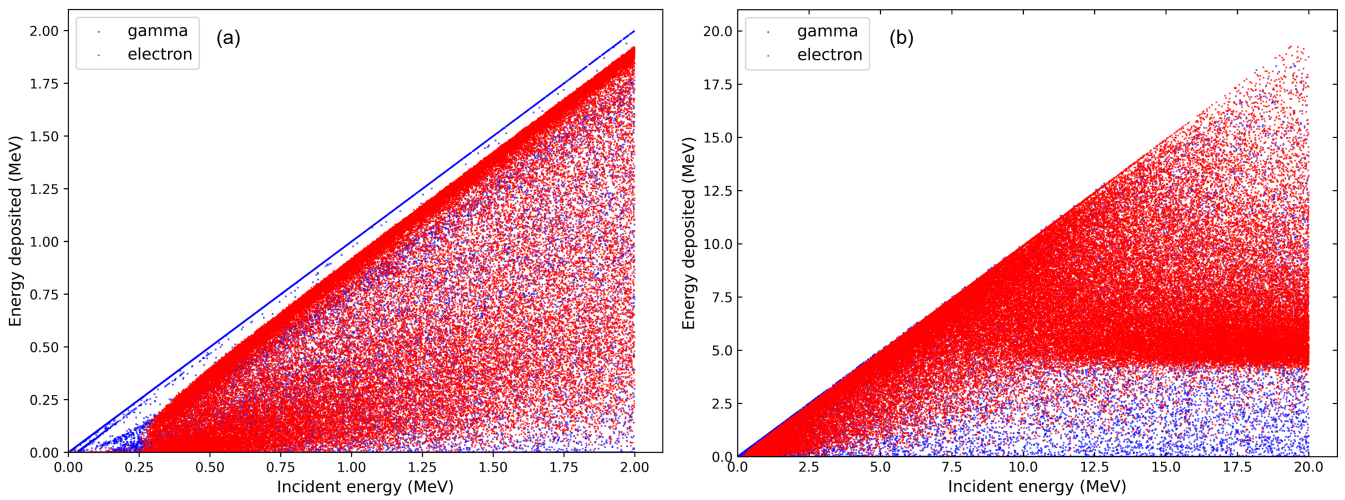


Fig. 11. Electron response matrix and gamma response matrix of the GTP for the narrow energy range of 0-2 MeV (a) and the wide energy range of 0-20 MeV (b).

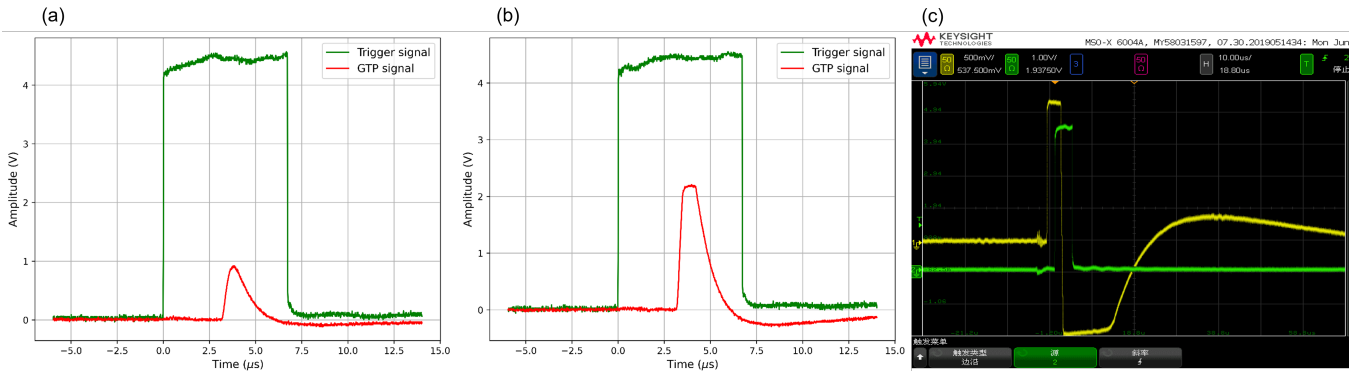


Fig. 12. Pulse waveform of the quasi-single electron beam on the GTP, which includes: normal event (a) and overflow events (b) and (c). Figure (c) shows a screenshot from the oscilloscope, where the yellow trace represents the overflow pulse signal generated by the 20 MeV electron beam on the GTP, while the green trace represents the trigger pulse signal.

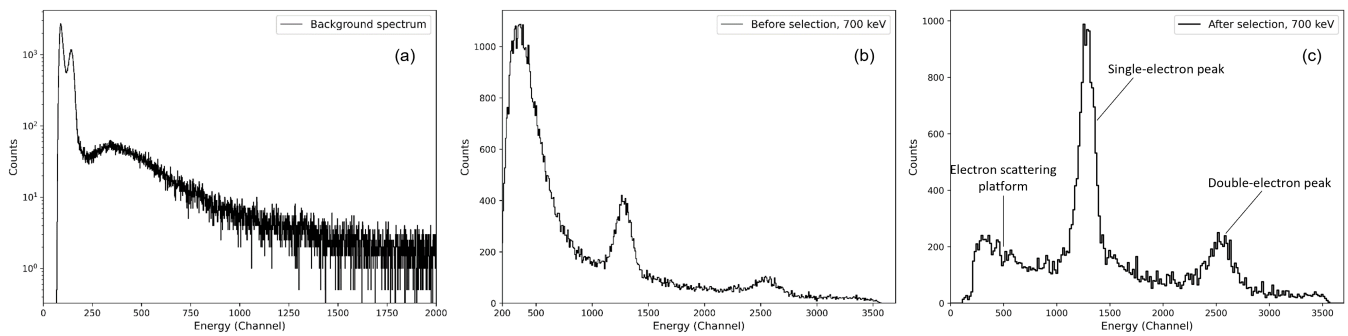


Fig. 13. (a) Background spectrum detected by the GTP. (b) Deposited energy spectrum before time interval selection of electron beam events. (c) Deposited energy spectrum after time interval selection of electron beam events.

fitted curve of the E-C relationship and considering the presence of a detection threshold as well as the channel limitations of the data acquisition system, we conclude that the GTP has an electron detection energy range of 310-1629 keV.

## V. SUMMARY

The GTM payload is a novel all-sky monitor specifically designed for gamma-ray detection in the 20 keV to 1 MeV

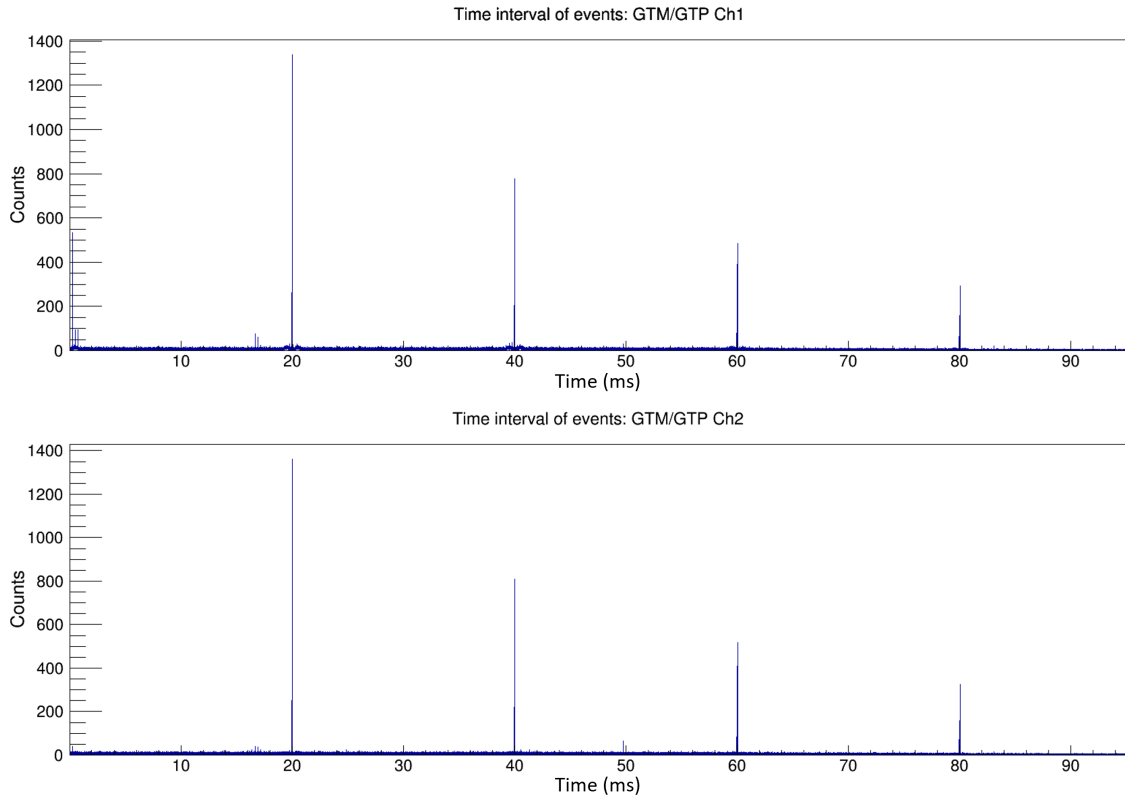


Fig. 14. Time interval spectrum of the selected 0.7 MeV electron beam at 50 Hz. Ch1 and Ch2 represent the two readout channels of the GTP.

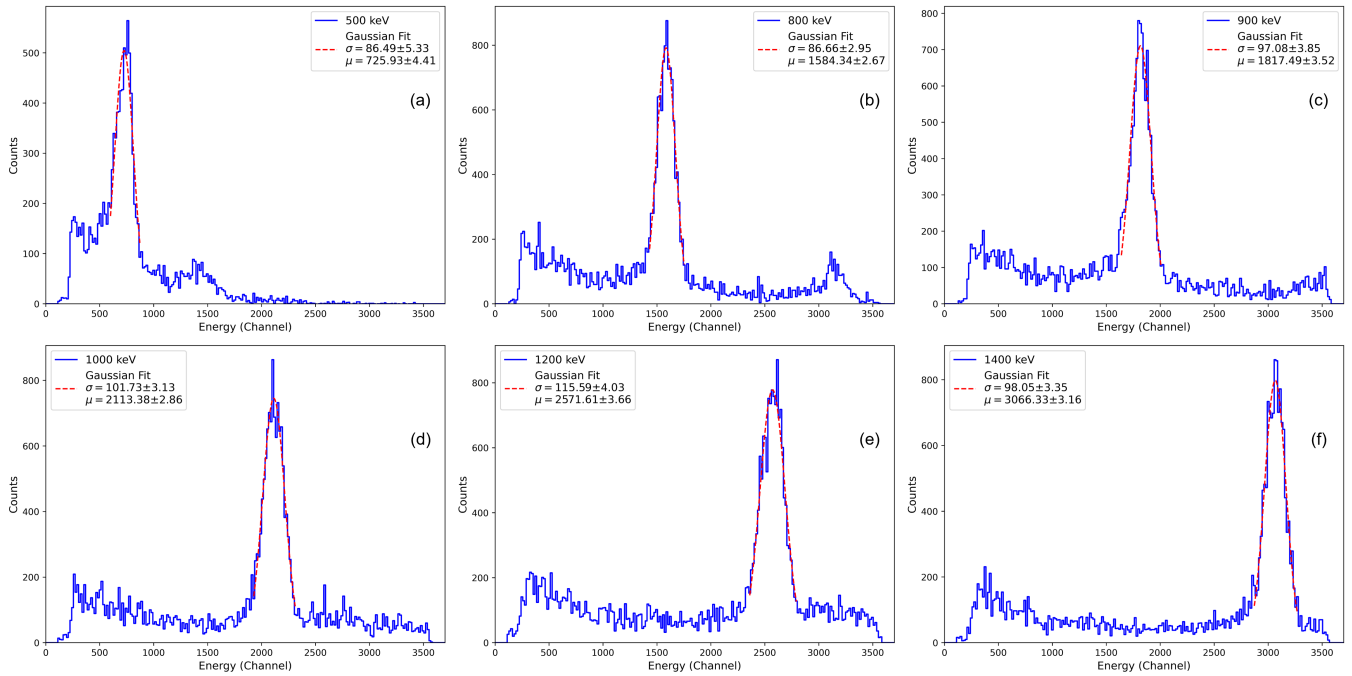


Fig. 15. Net deposited energy spectra of the GTP for 0.5 MeV (a), 0.8 MeV (b), 0.9 MeV (c), 1 MeV (d), 1.2 MeV (e), and 1.4 MeV (f) electron beams.

range, which was launched into the Distant Retrograde Orbit (DRO) in 2024. During its in-orbit operation, the GTM

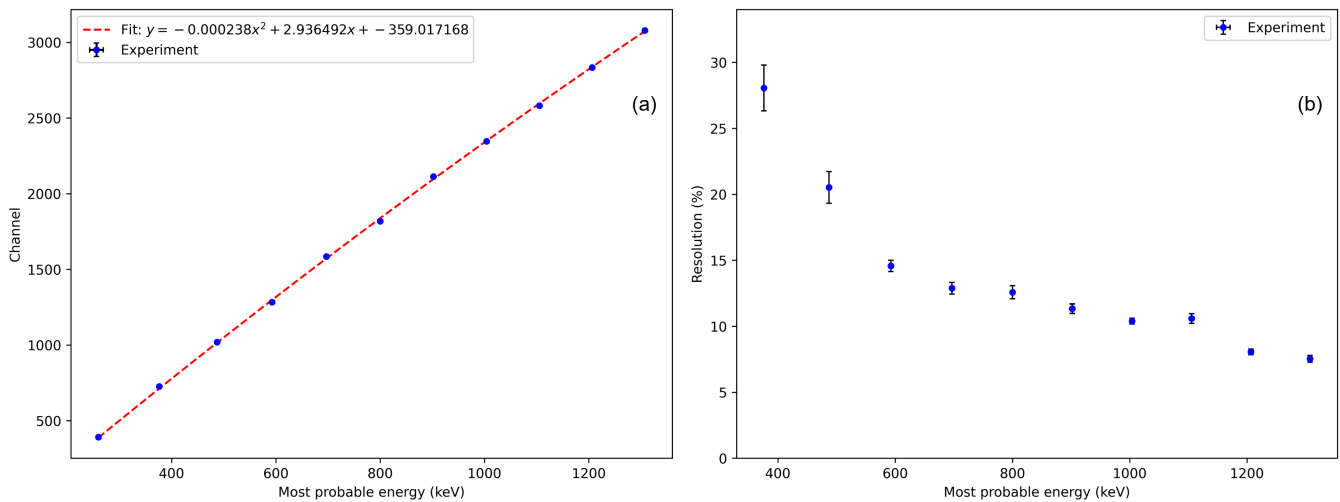


Fig. 16. (a) Energy-channel relationship of the GTP was established by fitting these data points with the quadratic polynomial. (b) Energy resolution of the GTP, with the uncertainties calculated using the error propagation formula..

encounters strong electron activity each month as it traverses the magnetotail region. In this study, we conducted formal ground-based electron calibration of the GTP using a unique domestic electron accelerator renowned for its low-current capability. We primarily tested the GTP's dead time for electron signals in the range of 0.4 to 20 MeV and the deposited energy spectrum in the range of 0.4 to 1.4 MeV. The results indicate that the GTP accurately records overflow events and performs as expected. We simulated the electron energy spectrum of the GTP with and without obstructive materials using Geant4, finding that electrons can only deposit energy in the GTP if they carry energy greater than 250 keV to penetrate the Be window and Teflon materials. The simulation results are consistent with the calibration findings. Considering the E-C relationship, detection threshold, and channel limitations of the data acquisition system, we conclude that the GTP has an electron detection energy range of 310 to 1629 keV. The ground-based electron calibration enhances the mass model of the detector and verifies its response in the high-energy range, laying the foundation for establishing a calibration database and representing a critical step in the development and operation of the GTM payload. Calibrating the efficiency of the GTP using electron beams is challenging due to electron scattering in the NaI(Tl) detector. We provide simulated results regarding the GTP's detection efficiency for electrons. Additionally, in future work, we plan to use a backup GTP

for proton calibration. Currently, the data acquisition program cannot relate the GTP signal width to energy. We recommend incorporating this functionality in upcoming engineering projects to expand the energy measurement range.

## VI. ACKNOWLEDGMENTS

This work is supported by the Strategic Priority Research Program of the Chinese Academy of Sciences (Grant No. XDA30050100) and the National Natural Science Foundation of China (Grant Nos. 12173038, 11775251, 12273042, and 12075258). The GECAM (Huairou-1) mission was funded by the Strategic Priority Research Program on Space Science (XDA15360000) of the Chinese Academy of Sciences (CAS). We thank the staff of the Shandong Institute of Aerospace Electronic Technology, National Institute of Metrology, for significantly helping in the development and ground calibration tests of the GTM. We also thank the DRO team.

## CONFLICT OF INTEREST

The authors declare that they have no competing interests.

- 
- [1] Benjamin P Abbott, Rich Abbott, TDea Abbott, et al. Gw170817: observation of gravitational waves from a binary neutron star inspiral. *Phys. Rev. Lett.*, 119(16):161101, 2017. doi: <https://doi.org/10.1103/PhysRevLett.119.161101>.
- [2] Benjamin P Abbott. Multi-messenger observations of a binary neutron star merger. *Astrophys. J. Lett.*, 848(2):L12, 2017. doi: <https://doi.org/10.3847/2041-8213/aa91c9>.
- [3] Benjamin P Abbott, Robert Abbott, TD Abbott, et al. Gravitational waves and gamma-rays from a binary neutron star merger: Gw170817 and grb 170817a. *Astrophys. J. Lett.*, 848(2):L13, 2017. doi: <https://doi.org/10.3847/2041-8213/aa920c>.
- [4] TiPei Li, ShaoLin Xiong, ShuangNan Zhang, et al. Insight-hxmt observations of the first binary neutron star merger gw170817. *Sci. China-Phys. Mech. Astron.*, 61:1–8, 2018. doi:

- <https://doi.org/10.1007/s11433-017-9107-5>.
- [5] Nicolas Arnaud. Ligo and virgo detector characterization and data quality: Contributions to the o3 run and preparation for o4. *Nucl. Instrum. Methods Phys. Res. Sect. A-Accel. Spectrom. Dect. Assoc. Equip.*, 1048:167945, 2023. doi: <https://doi.org/10.1016/j.nima.2022.167945>.
- [6] Ved G Shah, Gautham Narayan, Haille ML Perkins, et al. Predictions for electromagnetic counterparts to neutron star mergers discovered during ligo-virgo-kagra observing runs 4 and 5. *Mon. Not. R. Astron. Soc.*, 528(2):1109–1124, 2024. doi: <https://doi.org/10.1093/mnras/stad3711>.
- [7] RL Aptekar, DD Frederiks, SV Golenetskii, et al. Konus-w gamma-ray burst experiment for the ggs wind spacecraft. *Space Sci. Rev.*, 71:265–272, 1995. doi: <https://doi.org/10.1007/BF00751332>.
- [8] Neil Gehrels, Carl E Fichtel, Gerald J Fishman, et al. The compton gamma ray observatory. *Scientific American*, 269(6):68–77, 1993. doi: <https://doi.org/10.1086/191978>.
- [9] Neil Gehrels, Guido Chincarini, PE Giommi, et al. The swift gamma-ray burst mission. *Astrophys. J.*, 611(2):1005, 2004. doi: <https://doi.org/10.1086/422091>.
- [10] Charles Meegan, Giselher Lichti, PN Bhat, et al. The fermi gamma-ray burst monitor. *Astrophys. J.*, 702(1):791, 2009. doi: <https://doi.org/10.1088/0004-637X/702/1/791>.
- [11] Tatehiro Mihara, Mutsumi Sugizaki, Masaru Matsuoka, et al. Maxi: all-sky observation from the international space station. In *Space Telescopes and Instrumentation 2014: Ultraviolet to Gamma Ray*, volume 9144, pages 483–488. SPIE, 2014. doi: <https://doi.org/10.1117/12.2055792>.
- [12] Z. H. An, X. L. Sun, D. L. Zhang, et al. The design and performance of grd onboard the gecam satellite. *Radiat. Detect. Technol. Methods*, pages 1–10, 2022. doi: <https://doi.org/10.1007/s41605-021-00289-y>.
- [13] X. Q. Li, X. Y. Wen, Z. H. An, et al. The technology for detection of gamma-ray burst with gecam satellite. *Radiat. Detect. Technol. Methods*, pages 1–14, 2021. doi: <https://doi.org/10.1007/s41605-021-00288-z>.
- [14] P. Y. Feng, Z. H. An, D. L. Zhang, et al. Detector performance of the gamma-ray transient monitor onboard dro-a satellite. *Sci. China-Phys. Mech. Astron.*, 67(11):1–16, 2024. doi: <https://doi.org/10.1007/s11433-024-2458-9>.
- [15] Weimin Yuan, Chen Zhang, Yong Chen, et al. The einstein probe mission. In *Handbook of X-ray and Gamma-ray Astrophysics*, pages 1–30. Springer, 2022. doi: [https://doi.org/10.1007/978-981-16-4544-0\\_151-1](https://doi.org/10.1007/978-981-16-4544-0_151-1).
- [16] J-L Atteia, B Cordier, and J Wei. The svom mission. *International Journal of Modern Physics D*, 31(05):2230008, 2022. doi: <https://doi.org/10.1142/S0218271822300087>.
- [17] Panping Li, Qian-Qing Yin, Zhengwei Li, et al. Catch: chasing all transients constellation hunters space mission. *Exp. Astron.*, 55(2):447–486, 2023. doi: <https://doi.org/10.1007/s10686-022-09879-0>.
- [18] D. L. Zhang, X. L. Sun, Z. H. An, et al. Dedicated sipm array for grd of gecam. *Radiat. Detect. Technol. Methods*, 6(1):63–69, 2022. doi: <https://doi.org/10.1007/s41605-021-00299-w>.
- [19] D. L. Zhang, X. Q. Li, S. L. Xiong, et al. Energy response of gecam gamma-ray detector based on labr3: Ce and sipm array. *Nucl. Instrum. Methods Phys. Res. Sect. A-Accel. Spectrom. Dect. Assoc. Equip.*, 921:8–13, 2019. doi: <https://doi.org/10.1016/j.nima.2018.12.032>.
- [20] D. L. Zhang, X. Q. Li, X. Y. Wen, et al. Gain stabilization and consistency correction approach for multiple sipm-based gamma-ray detectors on gecam. *Nucl. Instrum. Methods Phys. Res. Sect. A-Accel. Spectrom. Dect. Assoc. Equip.*, 1027:166222, 2022. doi: <https://doi.org/10.1016/j.nima.2021.166222>.
- [21] Y. Zhao, W. C. Xue, S. L. Xiong, et al. Gecam localization of high-energy transients and the systematic error. *Astrophys. J. Suppl. Ser.*, 265(1):17, 2023. doi: <https://doi.org/10.3847/1538-4365/acafeb>.
- [22] D. L. Zhang, C. Zheng, J. C. Liu, et al. The performance of sipm-based gamma-ray detector (grd) of gecam-c. *Nucl. Instrum. Methods Phys. Res. Sect. A-Accel. Spectrom. Dect. Assoc. Equip.*, 1056:168586, 2023. doi: <https://doi.org/10.1016/j.nima.2023.168586>.
- [23] H. Sun, C. W. Wang, J. Yang, et al. Magnetar emergence in a peculiar gamma-ray burst from a compact star merger. *arXiv preprint arXiv:2307.05689*, 2023. doi: <https://doi.org/10.48550/arXiv.2307.05689>.
- [24] Pei-Yi Feng, Xi-Lei Sun, Zheng-Hua An, et al. The energy response of labr3(ce), labr3(ce,sr), and nai(tl) crystals for gecam. *Nucl. Sci. Tech.*, 2024. doi: <https://doi.org/10.1007/s41365-024-01383-8>.
- [25] Z. H. An, S. Antier, X. Z. Bi, et al. Insight-hxmt and gecam-c observations of the brightest-of-all-time grb 221009a. *arXiv preprint arXiv:2303.01203*, 2023. doi: <https://doi.org/10.48550/arXiv.2303.01203>.
- [26] C. Zheng, Y. Q. Zhang, S. L. Xiong, et al. Observation of grb 221009a early afterglow in x-ray/gamma-ray energy bands. *Astrophys. J. Lett.*, 962(1):L2, 2024. doi: <https://doi.org/10.3847/2041-8213/ad2073>.
- [27] Yan-Qiu Zhang, Hao-Xiang Lin, Shao-Lin Xiong, et al. Relation between the kev-mev and tev emission of grb 221009a and its implications. *Astrophys. J. Lett.*, 2024. doi: <https://doi.org/10.3847/2041-8213/ad6df8>.
- [28] C. W. Wang, J. Zhang, S. J. Zheng, et al. Simulation of the in-flight background and performance of dro/gtm. *Exp. Astron.*, 57(3):26, 2024. doi: <https://doi.org/10.1007/s10686-024-09946-8>.
- [29] X. Q. Li, X. Y. Wen, Z. H. An, et al. The gecam and its payload. *Sci. Sin.-Phys. Mech. Astron.*, 50(12):129508–, 2020. doi: <https://doi.org/10.1360/SSPMA-2019-0417>.
- [30] S. L. Xiong. Special topic: Gecam gamma-ray all-sky monitor. *Sci. Sin.-Phys. Mech. Astron.*, 50(12):129501–, 2020. doi: <https://doi.org/10.1360/SSPMA-2020-0457>.
- [31] P. Valente, B. Buonomo, and G. Mazzitelli. Diagnostics and upgrade of the dafne beam test facility (btf). *Nucl. Phys. B-Proc. Suppl.*, 150:362–365, 2006. doi: <https://doi.org/10.1016/j.nuclphysbps.2004.06.013>.
- [32] F. B. Bateman, M. F. Desrosiers, L. T. Hudson, et al. Nist accelerator facilities and programs in support of industrial radiation research. In *AIP Conf. Proc.*, volume 680, pages 877–880. American Institute of Physics, 2003. doi: <https://doi.org/10.1063/1.1619849>.
- [33] M. Krmar, Y. Teterev, A.G. Belov, et al. Beam energy measurement on linac-200 accelerator and energy calibration of scintillation detectors by electrons in range from 1 mev to 25 mev. *Nucl. Instrum. Methods Phys. Res. Sect. A-Accel. Spectrom. Dect. Assoc. Equip.*, 935:83–88, 2019. doi: <https://doi.org/10.1016/j.nima.2019.04.104>.
- [34] M. Raggi, V. Kozhuharov, P. Valente, et al. Performance of the padme calorimeter prototype at the daφne btf. *Nucl. Instrum. Methods Phys. Res. Sect. A-Accel. Spectrom. Dect. Assoc. Equip.*, 862:31–35, 2017. doi: <https://doi.org/10.1016/j.nima.2017.05.007>.

- [35] G. Ambrosi, S. Bartocci, L. Basara, et al. Beam test calibrations of the hepd detector on board the china seismo-electromagnetic satellite. Nucl. Instrum. Methods Phys. Res. Sect. A-Accel. Spectrom. Dect. Assoc. Equip., 974:164170, 2020. doi: <https://doi.org/10.1016/j.nima.2020.164170>.
- [36] D. L. Zhang, M. Gao, X. L. Sun, et al. Quality assurance test and failure analysis of sipm arrays of gecam satellites. Radiat. Detect. Technol. Methods, pages 1–8, 2022. doi: <https://doi.org/10.1007/s41605-021-00282-5>.
- [37] Pei-Yi Feng and Xi-Lei Sun. Sipm-based gamma-ray detectors of gecam. Nucl. Instrum. Methods Phys. Res. Sect. A-Accel. Spectrom. Dect. Assoc. Equip., page 169826, 2024. doi: <https://doi.org/10.1016/j.nima.2024.169826>.
- [38] W. Lu, L. Wang, Y. Yuan, et al. Monte carlo simulation for performance evaluation of detector model with a monolithic labr3 (ce) crystal and sipm array for  $\gamma$  radiation imaging. Nucl. Sci. Tech., 33(8):107, 2022. doi: <https://doi.org/10.1007/s41365-022-01081-3>.
- [39] X. Huyan, O. Naviliat-Cuncic, P. Voytas, et al. Geant4 simulations of the absorption of photons in csi and nai produced by electrons with energies up to 4 mev and their application to precision measurements of the  $\beta$ -energy spectrum with a calorimetric technique. Nucl. Instrum. Methods Phys. Res. Sect. A-Accel. Spectrom. Dect. Assoc. Equip., 879:134–140, 2018. doi: <https://doi.org/10.1016/j.nima.2017.10.061>.